Nano Research
2019, 12(11): 2749–2759

ISSN 1998-0124 CN 11-5974/O4
https://doi.org/10.1007/s12274-019-2509-2

Research Article

Enhanced CH_4 selectivity in CO_2 photocatalytic reduction over carbon quantum dots decorated and oxygen doping g-C_3N_4

Qian Li[1,2], Songcan Wang[3], Zhuxing Sun[4], Qijun Tang[1,2], Yiqiu Liu[1,2], Lianzhou Wang[3] (✉), Haiqiang Wang[1,2] (✉), and Zhongbiao Wu[1,2]

[1] *Key Laboratory of Environment Remediation and Ecological Health, Ministry of Education, College of Environmental and Resources Science, Zhejiang University, Hangzhou 310058, China*
[2] *Zhejiang Provincial Engineering Research Center of Industrial Boiler and Furnace Flue Gas Pollution Control, Hangzhou 311202, China*
[3] *Nanomaterials Centre, School of Chemical Engineering and Australian Institute for Bioengineering and Nanotechnology, The University of Queensland, Brisbane, QLD 4072, Australia*
[4] *School of Environmental Science and Engineering, Shanghai Jiao Tong University, Shanghai 200240, China*

Received: 22 June 2019 / **Revised:** 10 August 2019 / **Accepted:** 27 August 2019

ABSTRACT

Graphitic carbon nitride (g-C_3N_4, CN) exhibits inefficient charge separation, deficient CO_2 adsorption and activation sites, and sluggish surface reaction kinetics, which have been recognized as the main barriers to its application in CO_2 photocatalytic reduction. In this work, carbon quantum dot (CQD) decoration and oxygen atom doping were applied to CN by a facile one-step hydrothermal method. The incorporated CQDs not only facilitate charge transfer and separation, but also provide alternative CO_2 adsorption and activation sites. Further, the oxygen-atom-doped CN (OCN), in which oxygen doping is accompanied by the formation of nitrogen defects, proves to be a sustainable H^+ provider by facilitating the water dissociation and oxidation half-reactions. Because of the synergistic effect of the hybridized binary CQDs/OCN addressing the three challenging issues of the CN based materials, the performance of CO_2 photocatalytic conversion to CH_4 over CQDs/OCN-*x* (*x* represents the volume ratio of laboratory-used H_2O_2 (30 wt.%) in the mixed solution) is dramatically improved by 11 times at least. The hybrid photocatalyst design and mechanism proposed in this work could inspire more rational design and fabrication of effective photocatalysts for CO_2 photocatalytic conversion with a high CH_4 selectivity.

KEYWORDS

photocatalytic, CO_2 reduction, graphitic carbon nitride (g-C_3N_4), carbon quantum dot, oxygen doping

1 Introduction

The exhaustion of fossil fuel resources, accompanied by the excessive emission of CO_2, has stimulated worldwide research on the use of CO_2 as a feedstock for the production of value-added chemical fuels such as CO, CH_4, and CH_3OH [1–3]. Since the first attempt in 1979 by Inoue and coworkers [4], artificial photosynthesis has been extensively applied for CO_2 photocatalytic conversion, where CO_2 is photocatalytically reacted with a reducing agent of H_2O over the semiconductor materials to simultaneously realize energy regeneration and CO_2 reduction [5, 6]. Although tremendous progress has been made in this area, the efficiency of CO_2 photocatalytic conversion is still very low, and practical application remains infeasible owing to the complexity of the reaction process [7] as well as the astounding thermodynamic stability of the CO_2 structure [8]. Therefore, further exploration of highly efficient semiconductor photocatalysts is needed.

In recent years, graphitic carbon nitride (g-C_3N_4, CN), a metal-free semiconductor, has been widely applied for CO_2 photocatalytic conversion, owing to its intrinsic advantages such as visible-light response, excellent chemical stability, and tunable band structure. However, its photocatalytic performance is limited by severe charge recombination, limited CO_2 adsorption and active sites [9, 10], and sluggish surface reaction kinetics. Since heterojunctions can not only effectively facilitate the charge transport but also combine the advantages of the coupled semiconductors [11, 12], the construction of g-C_3N_4 based heterojunctions is generally adopted to address the delayed charge transfer issue [13]. The alignment of the crystal phase, band structures, and interfacial contact of the contacted materials are essential for the successful construction of heterojunctions [14]. Owing to the two-dimensional (2D) π-conjugated structure that is analogous to that of CN, carbon quantum dots (CQDs) (in an ethanol and H_2O_2 mixed solution) have been considered as an excellent candidate to form heterojunctions with CN [15]. The unique features of CQDs such as the broad solar spectrum utilization and superior electronic conductivity can promote the generation and separation of the photogenerated electron–hole pairs [16, 17]. In addition, CQDs are a fascinating cocatalyst that can lower the activation energy of some reactants. More excitingly, CO_2 molecules are preferentially adsorbed on the surface of CQDs through π–π interactions, leading to the destabilization and activation of CO_2 for the subsequent reactions [18], which is one of the crucial yet challenging steps during the CO_2 photocatalytic reduction process. In addition, accelerating the kinetics of the water oxidation reaction can not only consume the photogenerated holes, promoting the separation of the photogenerated carriers, but also release protons required for hydrocarbon formation in the photocatalytic reduction of CO_2. Nonmetal heteroatom (O, S, P) doping has been recognized as an efficient modification method

Address correspondence to Haiqiang Wang, haiqiangwang@zju.edu.cn; Lianzhou Wang, l.wang@uq.edu.au

for CN because it can tailor its electronic and band structures [19–22]. In particular, oxygen doping in CN can generate abundant defects and form a more positive valence band (VB) potential [21, 23], which is theoretically favorable for water oxidation. Thus, coupling CQDs with oxygen doped CN (OCN) may synergistically enhance the CO_2 photocatalytic reduction performance. However, how to homogeneously decorate CQDs on OCN with strong interfacial interactions to achieve excellent charge transfer and separation remains challenging [24].

Herein, a new type of CQD/OCN nanocomposites were prepared by a facile one-pot hydrothermal approach, in which CN was added into a mixed liquid precursor of CQDs composed of ethanol and hydrogen peroxide (H_2O_2). This method not only enabled the *in situ* homogeneous decoration of CQDs on the surface of CN with close point-to-face heterojunctions, but also oxidized CN to form OCN, with H_2O_2 not only acting as the precursor of carbon dots together with ethanol, but as the source of oxygen doping. The synthetic sources are inexpensive and environmentally benign, and the synthetic process is mild and simple, which are favorable for large-scale production. The obtained CQD/OCN nanocomposites all exhibited superior CO_2 photocatalytic reduction activity and the CH_4 production of the optimal sample CQD/OCN-25% was approximately 14 times higher than the CN benchmark. The roles of the CQDs and oxygen dopant in the composites were systematically investigated, and the underlying mechanism for the enhanced photocatalytic activity was proposed. The synergistic effect of CQDs and oxygen doping on promoting the CO_2 photocatalytic reduction performance of CN demonstrated in this work would inspire the design of efficient photocatalysts for solar fuel production.

2 Experimental

2.1 Catalyst preparation

All the chemical reagents used in this study were purchased from Sinopharm Chemical Reagent Co. Ltd. (Shanghai, China); they were of analytical purity and used without further purification.

CN was first synthesized by thermal polymerization of urea. Typically, 20 g of urea was placed in a 100 mL crucible with a full cover, which was placed in a muffle furnace that was heated to 550 °C at a programmed ramping rate of 10 °C·min^{-1} and held at that temperature for 2 h. After cooling down to room temperature, a yellow powder, i.e., CN, was obtained and held for further study. CQD-decorated and oxygen doped CN nanosheets were synthesized by hydrothermally treating the samples in an ethanol and H_2O_2 mixed solution. Specifically, 0.4 g of CN was added into a 200 mL Teflon-lined autoclave containing a certain volume of ethanol, followed by ultrasonication for 3 h to form a homogeneous suspension. Then, commercial H_2O_2 (30 wt.%) was added into the obtained suspension under vigorous stirring for 30 min, and the autoclave was then kept in a dry oven at 150 °C for 4 h. After adequate centrifugal washing of the product with ethanol and deionized water, an off-white powder was obtained. The total liquid volume was controlled at 140 mL. By adjusting the volume ratio of ethanol and H_2O_2, different quantities of CQDs were anchored on the surface of CN. The samples were denoted as CQD/OCN-*x*, where *x* represents the volume ratio (*v*%) between laboratory-used H_2O_2 (30 wt.%) and absolute ethanol. For comparison, CN powder was also subjected to the same treatment in the absence of H_2O_2 or with the deionized water replaced by ethanol to obtain eth-CN and OCN-*x* (*x* represents the volume ratio of deionized H_2O_2 and water), respectively. Pure CQDs were also prepared without adding CN. Further, 0.5 wt.%-CQD/OCN (denoted as p-CQD/OCN) was also synthesized as a reference by a post-combination method, in which CQDs were fabricated and mixed with OCN in ethanol for 24 h, followed by calcination at 300 °C for 1 h after drying. Note that, to eliminate the intrinsic carbonaceous impurities adsorbed on the surface of the samples, all the synthesized samples were vacuumed-treated at 130 °C using a static adsorption instrument before their photocatalytic performances were investigated.

2.2 Characterization methods

Scanning electron microscopy (SEM, UHR FE-SEM, SU 8010, Hitachi, Ltd., Japan) and transmission electron microscopy (TEM, H-600, Hitachi, Ltd., Japan) were performed to study the morphological structures of the samples. The physical structures of the as-synthesized samples were investigated by X-ray diffraction analysis (XRD, Model D/max RA, Rigaku Co., Japan, with Cu Kα radiation) and Fourier transform infrared (FTIR) spectroscopy (Nicolet 5700). Raman spectra were obtained using a micro-Raman spectroscope (LabRAM HR800, Horiba Jobin Yvon Co., France) with a 325 nm He–Cd ultraviolet laser as the exciting source. The chemical composition and surface properties were studied by X-ray photoelectron spectroscopy (XPS) with a monochromatic Al Kα source (150 W, 500 μm, 1,486.6 eV), and the binding energies were calibrated using the C 1s level at 284.6 eV as a reference. Nitrogen adsorption–desorption isotherms were obtained on a static adsorption instrument (JW-BK 132F, Beijing JWGB Sci & Tech Co., China). UV–visible absorption spectra were recorded on a spectrophotometer (TU-1901, China) equipped with an integrating sphere assembly, taking $BaSO_4$ as the reference. Photoluminescence (PL) spectra were acquired on a fluorescence spectrophotometer (FLS920, Edinburgh Instruments, UK), where a 325 nm laser and a xenon lamp were used as the light source. Photoelectrochemical characterizations, including transient photocurrent, alternating current (AC) impedance, and Mott–Schottky plots, were obtained on an electrochemical analyzer (CHI-660E, China) in a standard three-electrode system with Na_2SO_4 (0.2 M) as the electrolyte solution. Platinum wire (CHI115) and saturated Ag/AgCl (CHI111) were used as the counter electrode and reference electrode, respectively. The working electrodes were prepared using a piece of indium tin oxide (ITO) glass coated with our samples on an active area of 1 cm × 1 cm from a coating solution. The electron spin resonance (ESR) measurements were conducted at room temperature using a JES FA200 spectrometer (Japan). To be specific, solid samples (20 mg) were dispersed into an electron paramagnetic resonance (EPR) tube, then irradiated with a 300 W Xenon lamp equipped with a 420 nm light cut filter. 5,5-Dimethyl-1-pyrroline N-oxide (DMPO, 100 mM) was employed as a spin trap to detect hydroxyl radicals (•OH) and superoxide radicals ($\bullet O_2^-$), whereas 2,2,6,6-tetramethylpiperidine-1-oxyl (TEMPO, 200 μM) was used as a spin label to detect photogenerated electrons (e^-). Besides, methanol was used as the reaction solvents for the detection of $\bullet O_2^-$, while deionized water for •OH and e^- in an oxygen-free environment.

2.3 Photocatalytic performance

The CO_2 photocatalytic reduction performance was evaluated in a continuous-flow system, as reported in our previous works [25, 26]. Specifically, 50 mg photocatalyst was uniformly coated on the bottom of a stainless-steel cylindrical reactor. Then the reactor was covered with a quartz glass, allowing the transmission of visible light emitted by a 300 W xenon lamp (PLS-SXE300UV) equipped with a 420 nm light cut filter. Before the formal experiments, the reactor was purged by a pure CO_2 flow at a rate of 120 mL·min^{-1} through water bubbling to eliminate any gaseous impurities remaining in the system. Then the flow was modulated to a slow stream of 3 mL·min^{-1} until the surface of the photocatalyst coating reached a saturation coverage with CO_2 and H_2O. The temperature of the water bubbling and reactor was controlled at 30 °C to obtain a stable water content and simultaneously eliminate the effects of the external environmental. Then, the light was turned on for 8 h, during which the gaseous products were qualitatively and quantitatively monitored by gas chromatography (Agilent 7890A, USA) periodically (every 20 min)

using the standard curves. The gas chromatograph was equipped with three detection channels, each of which was connected to a quantitative loop, followed by a Porapak column, a DB-Wax column, and a combination of Porapak and 5A columns, and then went to two flame ionization detectors and one thermal conductivity detector, respectively.

Blank experiments were also conducted in the same system following identical procedures under conditions of no light, no photocatalyst, and replacing CO_2 with pure Ar (99.99%) to confirm the source of the products. The accumulated product yields were calculated by integrating the production rate over time. CO_2 conversion was defined as the summation of the amount of C in the detected C-containing products, and the selectivity of CH_4 was defined as the utilization efficiency of electrons for CH_4 formation in the total reacted electrons, as shown in the following equations:

$$CO_2 \text{ conversion} = 2n(CO) + 8n(CH_4) \quad (1)$$

$$S_{CH_4}(\%) = \frac{8n(CH_4)}{2n(CO) + 8n(CH_4) + 2n(O_2)} \quad (2)$$

3 Results and discussion

3.1 Physical properties

The XRD patterns of pure CN, eth-CN, CQD/OCN-*x*, OCN-*x*, and CQDs are shown in Fig. 1(a). All the CN-containing samples exhibit two characteristic diffraction peaks. The much stronger one at approximately 27.5° is attributed to periodic graphitic interlayer stacking of aromatic segments corresponding to the (002) facet, and the weaker one at 13° is assigned to in-plane repeating motifs of the tri-s-triazine units [27]. Although the core crystal structure of CN is maintained, the peak intensities of the CQD/OCN-*x* and OCN-*x* samples are severely reduced. In particular, the peak at 13° is barely recognizable, suggesting the loss of intralayer ordering and a decrease in the planar size of the CN layers [28, 29], caused by breaking of the hydrogen bonds in the in-plane framework [30]. In addition, the (002) peak also exhibits a negative shift, indicating a larger interlayer spacing and looser stacking of interlayers. This result suggests that a thinner layer structure, similar to that of the exfoliated CN nanosheets, was obtained after treatment [29]. Furthermore, the broad, flat (002) peak of the CQDs at 20.1° is difficult to observe in the CQD/OCN-*x* samples, probably because of the low CQD content and homogeneous CQD dispersion. For the same reason, the main characteristic peaks indexed to CQDs at ca. 797, 1,023, 1,391, 1,621, 1,702, and 3,417 cm^{-1} in the FTIR spectra of the CQD/OCN-*x* samples (Fig. 1(b)), corresponding to C–O, C–O, $-CH_3$, C=C, C=O, and –OH, respectively, can be barely distinguished. In addition, the characteristic breathing mode of triazine units (807 cm^{-1}), stretching modes of CN heterocycles (1,050–1,650 cm^{-1}), and broad stretching vibration modes of –NH (3,000–3,400 cm^{-1}) are clearly observed for all the samples, indicating that the skeleton structure of CN remained intact after the hydrothermal treatment [9, 31]. A magnified view of the FTIR spectra of CN heterocycles reveals that a series of peaks shift toward higher wavelengths. With the increase of H_2O_2 concentration, the shifts tend to be more pronounced, which is attributed to the introduction of oxygen atoms that replace the N atoms in CN, and the stronger electron-attracting ability of the oxygen atoms compared to the nitrogen atoms [32]. To better understand the structure of the as-prepared samples, Raman spectra were obtained using UV light as the excitation light source (Fig. 1(d)). Similar to the peaks in the FTIR spectra, the main Raman peaks for all the CN-containing samples are almost unchanged except for the intensity, suggesting that the core skeleton of CN is undamaged. Moreover, the Raman peak of the CQDs at 1,360 cm^{-1} appears for the CQD/OCN-*x* samples, clearly indicating the presence of CQDs [33]. However, the other

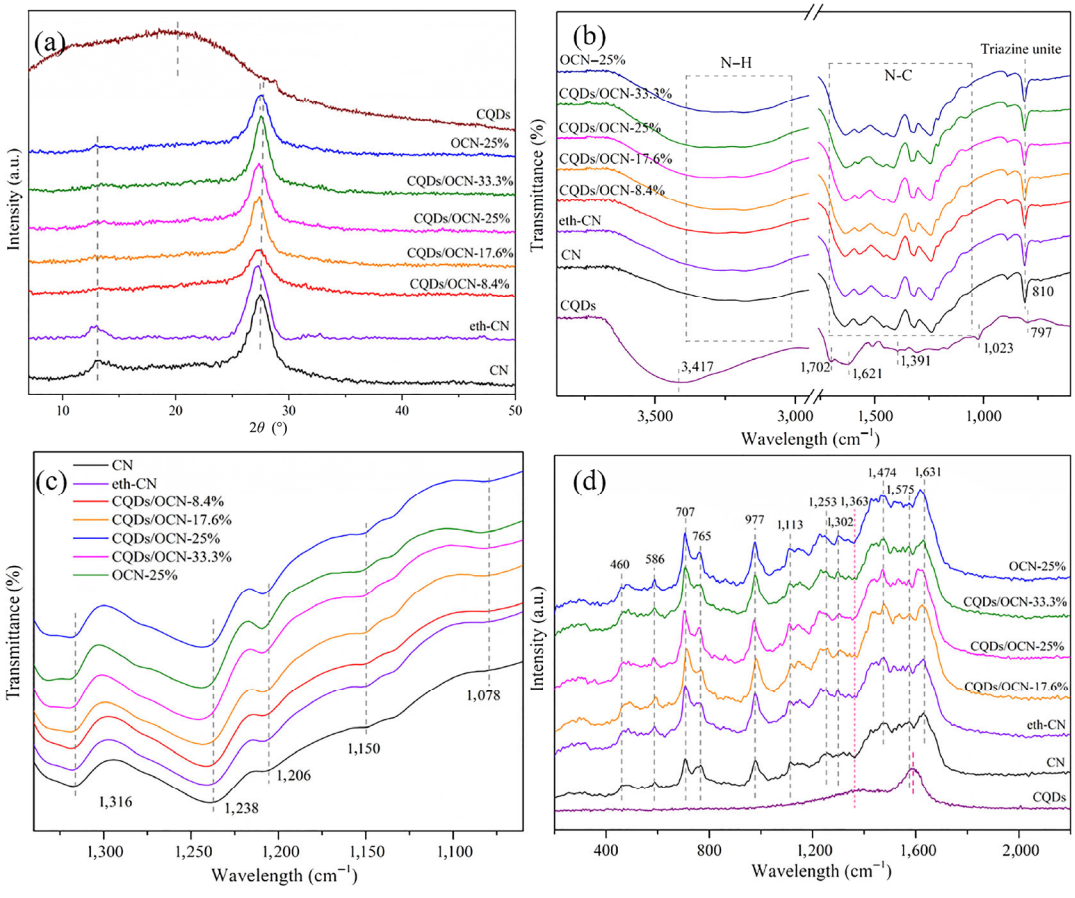

Figure 1 (a) XRD patterns, (b) transmittance FTIR spectra, (c) magnified view of part of FTIR spectra, and (d) Raman spectra of as-prepared samples.

Raman peak of CQDs at 1,590 cm^{-1} is almost invisible, probably because it overlaps in the CN peak centered at 1,575 cm^{-1}.

To directly observe the morphology and texture of the as-prepared samples, both SEM and TEM were employed. The SEM images (Fig. S1 in the Electronic Supplementary Material (ESM)) reveal that CN and eth-CN have almost identical morphologies, whereas CQD/OCN-*x* and OCN-25% exhibit nanoporous structures, and the pore size and the number increase with the H_2O_2 concentration, as clearly demonstrated by the pore size distribution and pore volume obtained from the N_2 adsorption–desorption isotherms (Fig. S2 in the ESM). The TEM images (Fig. 2) reveal the porosity of the samples, which is similar for all of the samples. Further, nanodots are visible in the high-resolution TEM (HRTEM) image of CQD/OCN-25% (Fig. 2(c)), although they are rather difficult to be observed owing to their very low content in the composites or the shadowing effect of CN. To further confirm the presence of CQDs, the supernatant of the as-prepared CQD/OCN-25% composite was collected after centrifugation and then purified and concentrated, after which a bright yellow solution was obtained. The solution was observed by TEM, and the results are shown in Fig. 2(f). Many nanodots with an average size of 5 nm are clearly visible. Distinct lattice stripes with a spacing of 0.28 nm can also be observed (Fig. S3 in the ESM), providing further strong evidence for the presence of CQDs in the CQD/OCN-25% composite. Furthermore, when the mixed solution of H_2O_2 and ethanol after the hydrothermal treatment was also subjected to the TEM morphology investigation, a large number of carbon quantum dots could be distinctly observed, which revealed that carbon quantum dots were the product of the hydrothermal reaction of H_2O_2 and ethanol. CQD incorporation and oxygen doping were further confirmed by XPS measurements. Figures 3(a) and 3(b)

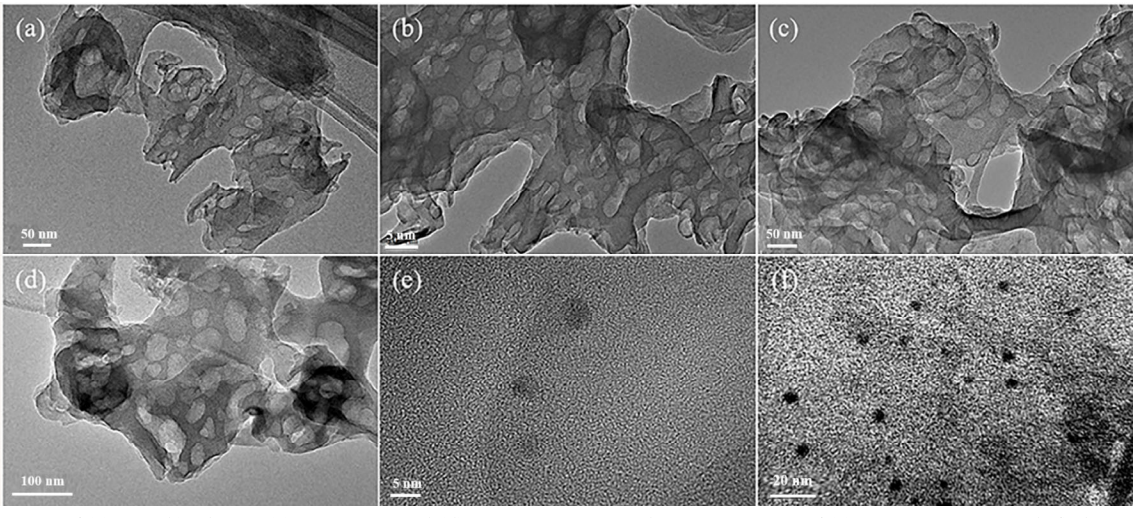

Figure 2 TEM images of (a) CN, (b) eth-CN, (c) OCN-25%, and (d) CQD/OCN-25% and HRTEM images of (e) CQD/OCN-25% and (f) the purified centrifugal supernatant of CQD/OCN-25%.

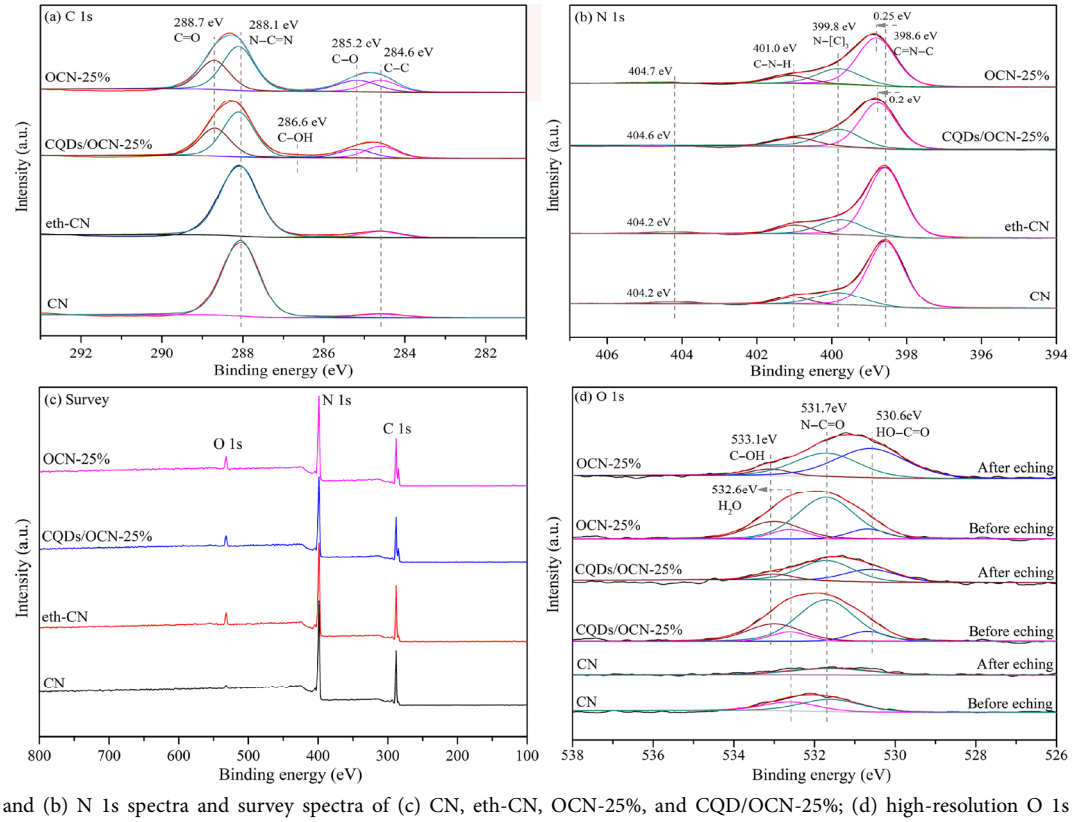

Figure 3 (a) C 1s and (b) N 1s spectra and survey spectra of (c) CN, eth-CN, OCN-25%, and CQD/OCN-25%; (d) high-resolution O 1s XPS spectra of CN, OCN-25%, and CQD/OCN-25% before and after etching.

show the C 1s and N 1s XPS spectra of CN, eth-CN, QD/OCN-25%, and OCN-25%. The C 1s spectra of CN and eth-CN are almost identical; the characteristic peak at 288.1 eV is assigned to sp^2 N–C=N bonds in the tri-s-triazine rings, where the adventitious carbon peak at 284.6 eV is used for calibration. Further, two new peaks at 285.2 and 288.7 eV emerged when the C 1s XPS spectra of CQD/OCN-25% and OCN-25% were deconvoluted. They are ascribed to C–O [34] and COOH [35], respectively, resulting from the deep oxidation of the sp^2-hybridized carbon by H_2O_2. The C–OH peak centered at 286.6 eV can be observed only for CQD/OCN-25%, which is originated from the surface hydroxyl groups of the CQDs [36, 37]. All the samples exhibit similar N 1s XPS profiles with four characteristic peaks. The weak peak located at 404.2 eV for CN and eth-CN, which is ascribed to π–π^* excitation of the C–N conjugated structure, shifting to 404.6 and 404.7 eV for CQD/OCN-25% and OCN-25%, respectively, which indicates that the π electrons are damaged as the layer is destroyed [9]. The other four peaks centered at approximately 398.6, 399.8, 401.0, and 404.3 eV are ascribed to sp^2-hybridized nitrogen (C–N=C), sp^3 hybridized nitrogen (N–[c]$_3$), and C–NH_x [38], respectively. The atomic ratios of nitrogen species are summarized in Table 1, which shows that the atomic ratio between C–N=C and N–[c]$_3$ decreases. This result, combined with the distinctly higher binding energy shifts of the peaks for C–N=C in CQD/OCN-25% and OCN-25% (Fig. 3(b)), suggests that the sp^2-hybridized nitrogen may be replaced by O atoms with a stronger electric negativity. Direct evidence of O doping is also obtained from the XPS survey spectra and the O 1s XPS spectra. First, in the XPS survey spectra (Fig. 3(c)), the O 1s peaks of CQD/OCN-25% and OCN-25% are much more intense than that of CN and eth-CN, indicating the introduction of more oxygen functional groups after H_2O_2 treatment. Table S1 in the ESM shows the oxygen atomic contents obtained from the full-scan XPS spectra taken after the surface was etched to a depth of 5 nm. The peak at 532.6 eV in the O 1s high-resolution XPS spectra (Fig. 3(d)) is assigned to surface-adsorbed water [39]. After etching, one weak peak centered at 531.7 eV remains for CN, which corresponds to isocyanic acid or other residual oxygen-containing intermediate species formed during the calcination of urea [40, 41]. For CQD/OCN-25% and OCN-25%, peaks centered at 531.7 are assigned to N–C–O [38, 42], and those at 530.6 and 533.1 eV are respectively attributed to HO–C=O and C–OH [43–45]. The three kinds of peaks always present could be observed before and after etching, indicating that these oxygen-containing groups are uniformly dispersed in the matrix, rather than from surface adsorbed impurities. In particular, the presence of N–C–O clearly confirms the replacement of the sp^2-hybridized N atoms by O atoms. Considering that there are three possible substitution sites for the N atoms in CN, as shown in Fig. S4 in the ESM, density functional theory computation was used to compare the energies of the three possible geometries of CN after substitution. A geometry with a lower energy generally indicates a more stable structure. The results demonstrate that two-coordinated N atoms are preferentially replaced by O atoms, which exhibits the lowest energy of −473.3 eV, in line with the previously studies [19, 32].

Table 1 Atomic ratios of nitrogen species in CN, eth-CN, CQD/OCN-25%, and OCN-25%

Samples	Nitrogen species (at.%)		
	C–N=C	N–[c]$_3$	C–NH_x
CN	75.84	20.73	3.43
eth-CN	72.57	18.75	8.68
CQDs/OCN-25%	61.85	25.57	12.58
OCN-25%	64.54	24.37	11.10

3.2 CO_2 photocatalytic reduction performance

The CO_2 photocatalytic reduction activity of the as-prepared samples was evaluated under visible light (λ > 420 nm) irradiation. For all the samples, the main products detected were CH_4 and CO. H_2 and other organic products, such as CH_2OH and HCOOH et al., were basically not detected, probably due to their very low production. Control experiments in the absence of catalysts and light or using N_2 instead of CO_2 were first conducted and presented negligible product yields, which confirm that the products are generated from the photocatalytic reduction reactions between CO_2 and H_2O, rather than any other carbonaceous impurities. The cumulative CO production in 8 h over all the samples is presented in Fig. S5(a) in the ESM. The CO production over the CQD/OCN-*x* samples increases gradually when increasing the CQD content, but it is much lower than that over CN, except for the CQD/OCN-33.3% sample. In contrast, the CH_4 production over the CQD/OCN-*x* samples increased remarkably compared with that of their CN counterparts regardless of the CQD content (Fig. 4(a)). Notably, optimal CH_4 production was obtained over CQD/OCN-25%, achieving a yield of 1.2 $\mu mol \cdot g^{-1}$, which is nearly 14 times higher than that of pure CN. CQD/OCN-25% also shows the best total CO_2 conversion in 8 h, with a production yield of 13.83 $\mu mol \cdot g^{-1}$, which is approximately 2.5 times that of CN (Fig. S5(b) in the ESM). CO_2 photocatalytic reduction tests of eth-CN and OCN-25% were also conducted for comparison. The CH_4 production of both samples shows no significant improvement compared with that of CN, which not only suggests that ethanol or H_2O_2 treatment of CN alone do not greatly affect the CO_2 photocatalytic reduction performance, but also confirms the effective role of CQDs in the enhancement of CH_4 production. Ultimately, the CH_4 selectivity of all the CQD/OCN-*x* samples reaches as high as ~ 70%, which is much higher than that of CN and OCN-25% (only 11.1% and 24.2%, respectively; Fig. 4(b)). Further, both the CH_4 production and selectivity of CQD/OCN-*x* are much higher than those of p-CQD/OCN, which demonstrates the superiority of the *in situ* decoration of CQDs on CN, as demonstrated in this study. In addition, to investigate the stability of the CO_2 photocatalytic performance over CQD/OCN-25%, long-duration experiments were conducted for three continuous runs, and then the samples were thoroughly washed and carefully recycled for three times for a fresh photocatalytic experiment to study their regenerative performance. The results are presented in Fig. 4(c). The yield of CH_4 gradually decreases in the first three consecutive tests, which is a common and acceptable behavior that can be attributed to the occupation of reactive sites caused by the accumulation of the intermediate products, as clearly demonstrated by the restoration of CH_4 production after adequate washing. The FTIR spectra (Fig. 4(d)) of the sample before and after the photocatalytic reactions were almost identical, which reveals the excellent stability of the physical structure. Elaborate observation finds that the FTIR peaks at 1,079, 1,151, and 1,208 cm^{-1} become a little stronger, which are respectively assigned to carboxylic groups [46], C–O stretching vibration [47, 48] and weakly held carbonates [49]. And these observations may account for the drop of CO_2 photocatalytic reduction activity in the continuous 3-runs experiments. Considering the greatly enhanced CH_4 production of CQD/OCN-25% as well as its excellent stability, a series of characterizations were employed and analyzed in detail to explore the mechanism underlying such enhancement.

3.3 Adsorption and activation of CO_2 and CO

It is widely acknowledged that adsorption and activation of the targeted gas on the surface of a catalyst are crucial for the subsequent photocatalytic reactions [3]. The CO_2 adsorption content and CO_2 temperature-programmed desorption (TPD) profiles were therefore obtained. As shown in Fig. 5(a), only one CO_2 desorption peak can

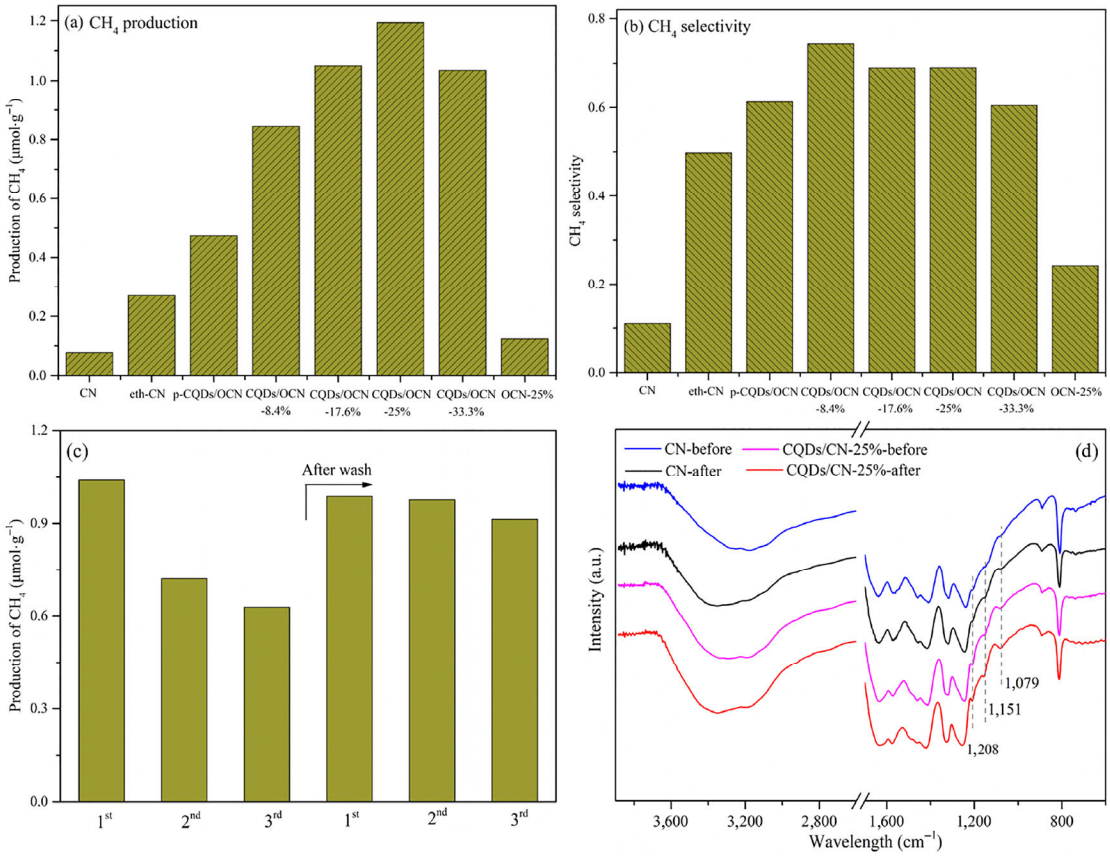

Figure 4 (a) Cumulative 8 h CH_4 yields and (b) CH_4 selectivity over CN, eth-CN, p-CQD/OCN, OCN-25%, and CQD/OCN-*x*; (c) results of repeated and recycling tests of CQD/OCN-25% under visible light irradiation; and (d) comparison of FTIR spectra of CN and CQD/OCN-25% before and after photocatalytic reactions.

be observed in CN and eth-CN with the adsorption temperature centered at ~ 445 °C. In contrast, the intensity of the CO_2 desorption peak in OCN-25% is much higher. As for CQD/OCN-25%, the desorption peak between 150 and 500 °C is wide and flat, possibly owing to superposition of several different peaks derived from the adsorption on CN and CQDs. The main peak is centered at 374 °C, which is much lower than the other three, indicating a more favorable activation process over CQD/OCN-25% [50, 51]. This phenomenon is probably attributable to the presence of CQDs. According to previous reports, CO_2 can be adsorbed on the surface of CQDs through π–π conjugation due to its delocalized π-conjugated II_3 bonding, thus facilitating the activation and delocalization of CO_2 [18, 52]. Further, a weak peak at ~ 96 °C emerges in both CQD/OCN-25% and OCN-25%, corresponding to the strong physically adsorbed CO_2 on the relatively weak basic sites [53, 54]. In addition, a peak at ~ 220 °C, which is attributed to the weak chemical adsorption of CO_2, appears only over OCN-25%. Further, judging from the peak intensity of all the samples, it could be roughly concluded that the adsorption content of CO_2 follows the order of OCN-25% > CQD/OCN-25% > eth-CN > CN. This is more precisely demonstrated by the CO_2 adsorption curves shown in Fig. 5(b). The greater CO_2 adsorption capacity of OCN-25% is attributed to its higher surface area and larger number of mesopores, as confirmed by the typical H_3 hysteresis loops in the nitrogen adsorption–desorption isotherms (Fig. S2 in the ESM) and by the Brunauer–Emmett–Teller surface area S_{BET}, the average pore sizes and pore volume, which are summarized in the inset table in Fig. S2 in the ESM. Note that the surface area, pore size, and pore volume of eth-CN are smaller than those of CN, but eth-CN exhibites much stronger CO_2 adsorption ability, which may have been due to the surface hydroxyl groups in eth-CN [55].

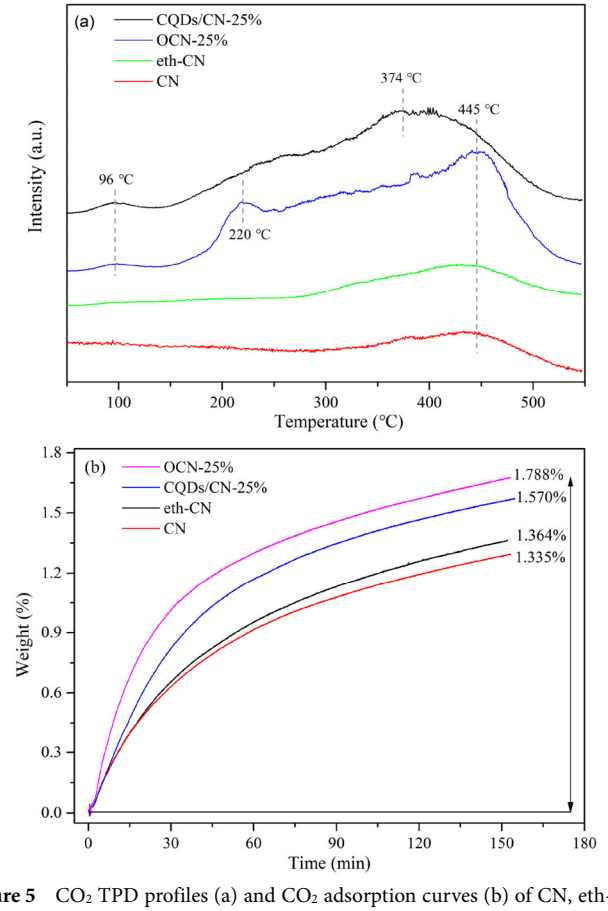

Figure 5 CO_2 TPD profiles (a) and CO_2 adsorption curves (b) of CN, eth-CN, OCN-25%, and CQDs/OCN-25%.

Considering that the photocatalytic products of all samples including CO and CH_4 but with different selectivity toward CH_4, CO-TPD profiles were thus collected, as CO may be served as an important intermediate. As displayed in Fig. S6 in the ESM, almost no CO desorption peaks are observed for CN and eth-CN, and the CO desorption temperatures of all OCN containing samples show no obvious difference at ~ 470 °C, assigning to the strong chemisorbed CO on the surface of OCN. Besides, the CO desorption peak intensity of CQDs/OCN-25% presents to be the best among all the CQDs-modified samples, and the adsorbed CO can accept electrons and participate in subsequent reactions.

3.4 Light absorption, charge separation, and carrier lifetime

UV–vis diffuse reflectance spectra of the as-prepared samples were obtained to investigate their optical properties, as shown in Fig. 6(a). The absorption edges of the eth-CN, OCN-25%, and CQD/OCN-*x* samples are clearly blue-shifted compared with that of pristine CN, indicating larger band gaps after hydrothermal treatment, in accordance with the color change from pale yellow (CN) to off-white (CQD/OCN-*x*) shown in the inset of Fig. 6(a). This phenomenon is attributed not only to the well-known quantum confinement of the nanosheets induced by the hydrothermal treatment, but also to the decrease in the conjunction degree of the CN structure accompanied by the formation of the in-plane holes [56]. In addition, many studies have reported that the introduction of carbon dots could improve the light absorbance of CN in the visible light region, although this improvement was not realized in our study, probably owing to the low CQD content of the CQD/OCN-*x* samples and the fact that the CQDs were partly oxidized by excess H_2O_2 during the synthetic process, resulting in the inferior light-harvesting properties [57, 58].

The wider band gaps are further reflected in the hypochromatic shift in the PL spectra (Fig. 6(b)) collected under excitation at 325 nm, which is also due to the quantum confinement effect. Further, it is noteworthy that the PL intensities of eth-CN and OCN-25% are much lower than that of CN, whereas the PL intensities of the CQD/OCN-*x* samples exhibit the opposite behavior and increase monotonically with the CQD concentration. Two factors may account for this behavior. One is that CQD/OCN-*x* samples can effectively reduce the non-radiative charge recombination rates [59, 60]. The second reason may be attributed to the quantum size effect of CN after hydrothermal treatment with ethanal and H_2O_2, during which the pristine CN powder could be delaminated to few layers, evidenced by the color change of samples and enlarged bandgaps. Besides, the atomic microstructure images shown in Fig. S7 in the ESM also show that the thickness of CN powders is reduced after hydrothermal treated with H_2O_2 and ethanol.

The photocurrents of CN, eth-CN, OCN-25%, and CQD/OCN-25% were examined to investigate the dynamics of electron transfer, the intensity of which is usually determined by the quantity and charge separation efficiency of the photogenerated charges. As shown in Fig. 6(c), the photocurrents of eth-CN, OCN-25%, and CQD/OCN-25% are unexpectedly smaller than that of their CN counterpart, which may be attributed to the inferior light absorption (Fig. 6(a)) and increased impedance of electron transfer to the working electrode and/or the electrolyte [59, 60]. The incremental electron transfer resistance is directly verified by the larger radius of the semicircular region in the Nyquist plots obtained by electrochemical impedance spectroscopy (Fig. S6(a) in the ESM), which is considered to be related to the damage of the π-conjugated system and the formation of the nitrogen defects, as defects can capture electrons and thereby inhibit the electron transport [61]. In this view, the electron transfer resistance would increase as the number of defects increase, which is consistent with the EPR spectra of all the samples (Fig. S6(b) in the ESM). Note that the photocurrent of CQD/OCN-25% is much higher and the electron transfer resistance is lower than those of OCN-25%; both of these findings demonstrate the pivotal role of

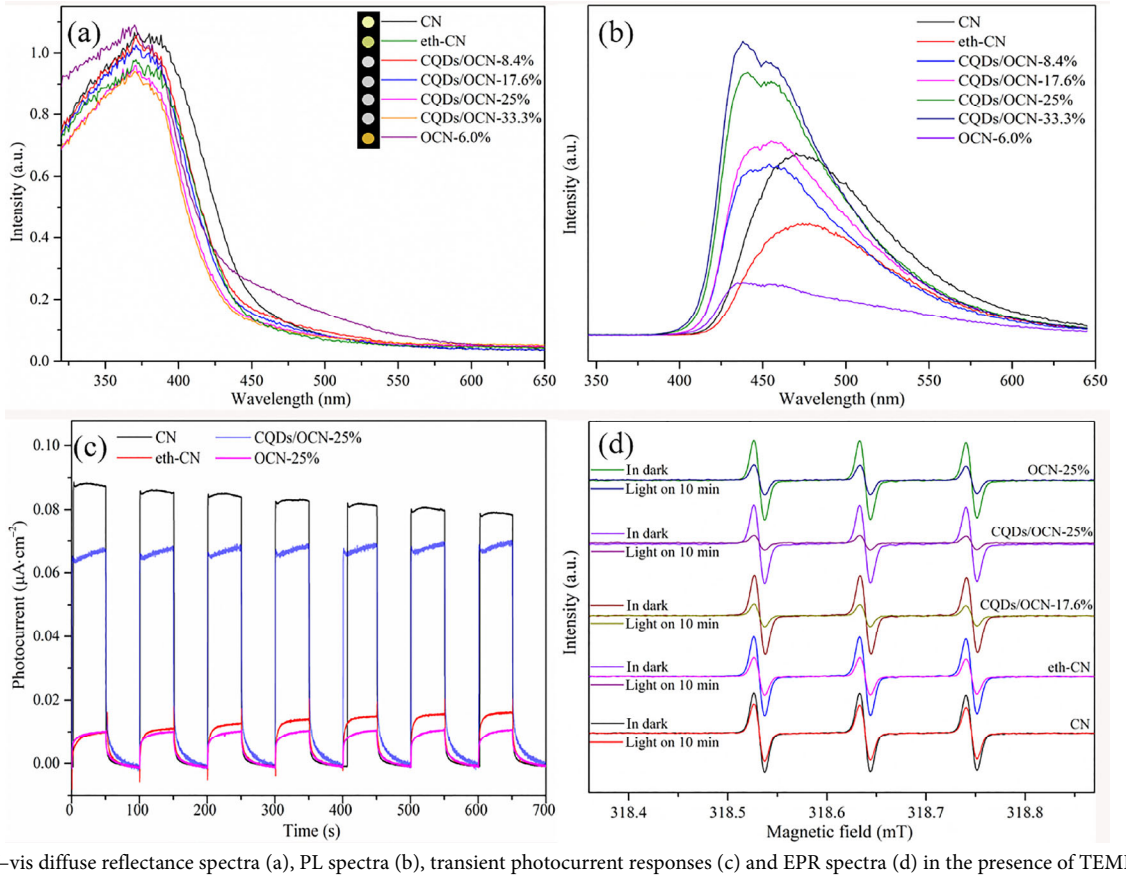

Figure 6 (a) UV–vis diffuse reflectance spectra (a), PL spectra (b), transient photocurrent responses (c) and EPR spectra (d) in the presence of TEMPO under visible light irradiation for CN, eth-CN, OCN-25%, and CQDs/OCN-*x*.

CQDs in facilitating the separation of the photoexcited charge carriers. Actually, the generation and subsequent transfer of the photoexcited charges occur after the saturated adsorption of the reactants during the photocatalytic reactions, which implies that the electrons captured by the defects are very likely to react with the reactants pre-adsorbed at the defect sites before they recombine with the photoexcited holes, thereby enhancing the utilization efficiency of the photoexcited electrons. To confirm this idea, EPR spectroscopy in the presence of TEMPO, a characterization technique for investigating the photoinduced electrons, was performed to simulate the photocatalytic reaction process, as shown in Fig. 6(d). The reduction in intensity and flattening of the EPR spectra are generally positively related with the quantities of the photoinduced electrons [63]. As shown in Fig. 6(d), visible-light irradiation leads to a distinct reduction in the TEMPO signals, revealing the effective electron transfer from the photocatalyst to TEMPO. As expected, the signal reduction over eth-CN, OCN-25%, and CQD/OCN-*x* is more distinct than that over CN, although CN exhibits the highest photocurrent among all the tested samples. This result indicates that the electrons trapped in the defects can react promptly with TEMPO before annihilation, in accordance with our proposed idea. In addition, the more remarkable signal reduction over CQD/OCN-*x* than over OCN-25% reveals the excellent utilization efficiency of the photoinduced electrons over CQD/OCN-*x*, confirming the efficient electron transfer efficiency induced by CQDs, in agreement with the photocurrent results (Fig. 6(c)).

3.5 Proposed photocatalytic mechanism

The information about the band-edge positions of the semiconductors is very important to understand the photocatalytic mechanism, which determines the likelihood of the photocatalytic reactions thermodynamically [3]. Thus, Mott–Schottky plots were obtained, from which the flat-band potential (V_{fb}) could be obtained as the *x* intercept of the linear portion. Figure 7(a) shows that all the tested samples are n-type semiconductors, judging from the positive slopes, and the V_{fb} values of all the samples are almost the same, with a value of −0.97 V (vs. Ag/AgCl, at pH = 7). Because the conduction band (CB) position is widely acknowledged to be approximately 0.3 V more negative than V_{fb} for n-type semiconductors [64], the CB position of all the samples could be calculated to be −1.07 V (vs. the normal hydrogen electrode (NHE) at pH = 7) from the Nernst equation, $E_{NHE} = E_{Ag/AgCl} + 0.197$ V [65]. Furthermore, the band gap energy (E_g) could be calculated from the UV–vis spectra (Fig. 6(a)) using the equation $E_g = 1{,}240/\lambda_g$, where λ_g represents the absorption edge of a semiconductor. Further, the VB positions (E_{VB}) could then be obtained using the formula $E_{VB} = E_g - E_{CB}$; the results are summarized in Table S2 in the ESM. The increase in band gap is assigned to the positive shift of the VB positions, which is probably induced by oxygen doping and is consistent with the experimental and computational results in the previous studies [21].

Fortunately, the slight expansion of the band gap would not affect the absorption of the visible-light photons (~ 2.95 eV). Thus, the photogenerated charge carriers would be produced once visible light is applied to the system; then the photogenerated electrons could be quickly transferred to the defect sites or the surface of the CQDs to react with the pre-adsorbed and immobilized CO_2 before recombination. Further, the photogenerated holes would react with the surface-adsorbed water molecules or hydroxyl groups to form •OH and $•O_2^-$ radicals, along with H^+ [66], which subsequently participates in reduction of the adsorbed CO_2 to produce hydrocarbons.

Note that •OH, which theoretically should not be produced because VB energies of the obtained photocatalysts are lower than the standard potential of •OH/H_2O (2.27eV vs. NHE) and •OH/OH^- (1.99 eV vs.

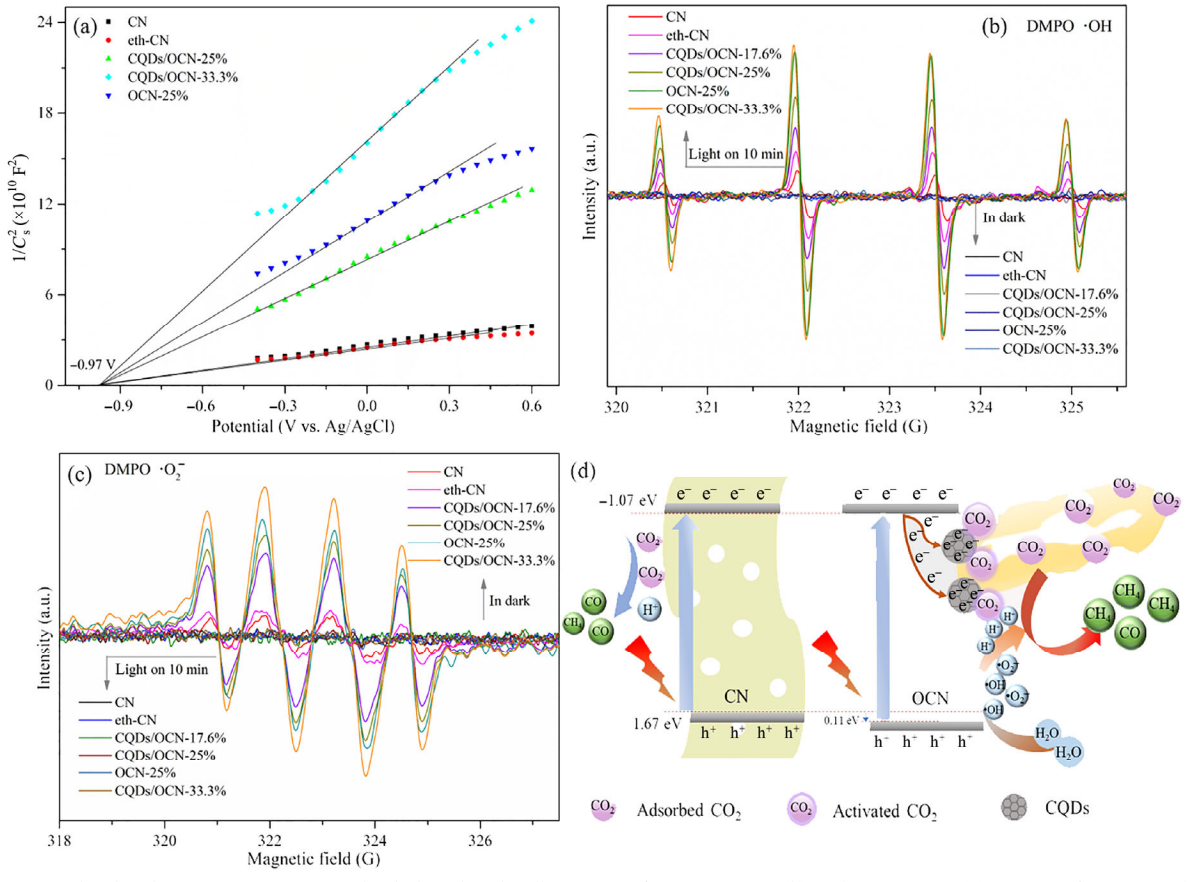

Figure 7 (a) Mott–Schottky plots (a), ESR spectra in the dark and under illumination for DMPO ·OH (b) and DMPO ·O_2^- (c) systems of as-prepared samples; and the schematic mechanism of CO_2 photocatalytic reduction over CQDs/OCN-*x* under visible light irradiation (d).

NHE), was surprisingly detected from the ESR results (Fig. 7(b)). Since the UV–vis spectra of the filtrate of fresh CQDs/OCN-25% shown in Fig. S9 in the ESM demonstrates that the detected •OH comes from the H_2O molecules rather from the residual H_2O_2 precursor. Then the phenomenon may be explained by the presence of defects, which are capable of enhancing the dissociation of the adsorbed H_2O molecules and thereby reducing the energy barrier of the reactions between the holes and H_2O to produce •OH [62, 67]. This could be further validated by the analogous trend in the variation of the intensity between the •OH radicals (Fig. 7(b)) and defects (Fig. S6(b) in the ESM). Further, as the generation of H^+ is virtually simultaneous with the formation of ·OH and $\bullet O_2^-$ radicals via the reactions $H_2O + h^+ \rightarrow H^+ + \bullet OH$ and $2\bullet OH + h^+ \rightarrow \bullet O_2^- + H^+$ [66, 68, 69], it is thus reasonable to consider that the evolution of H^+ over CQD/OCN-25% is far more abundant than that over CN. This can not only be judged from the much stronger intensity of the •OH and $\bullet O_2^-$ radicals over CQD/OCN-25% compared to that over CN, but also directly proved by the production of H^+ shown in Fig. S10 in the ESM. The sustainable supply of H^+ undoubtedly provides an important prerequisite for the evolution of CH_4, whose formation requires eight H^+ for each molecule according to the equation $CO_2 + 8H^+ + 8e^- \rightarrow CH_4 + 2H_2O$, thus accelerating the reaction kinetics at the same time. In sum, because the surface of the CQDs have a high electron density as well as ample CO_2 adsorption sites, and OCN acts as a stable supplier of H^+, CH_4 production over CQD/OCN-*x* is remarkably enhanced. The main processes of CO_2 photocatalytic reduction on CQD/OCN-*x* according to the analyses above are schematically illustrated in Fig. 7(d).

4 Conclusions

To improve the CO_2 photocatalytic reduction performance of CN as a metal-free semiconductor, CQD decoration and oxygen atom doping were simultaneously introduced via a facile, mild one-step hydrothermal treatment of CN with ethanol and H_2O_2. CQDs act as a co-catalyst, facilitating charge separation and transfer and thus increasing the electron density around the CO_2 adsorption sites. Thus, the CO_2 activation and delocalization are enhanced via π–π conjugation adsorption. Oxygen doping of CN leads to a more positive VB potential and abundant defects, facilitating dissociation of H_2O, providing more H^+. Because each component of the CQD/OCN-*x* complex performs indispensable functions, enhanced CH_4 production over CQD/OCN-*x* is realized. The CQD/OCN-25% sample exhibits the best performance; its CH_4 production is 14 times higher than that of CN. Moreover, cycling tests demonstrate the performance stability of the catalyst. The facile synthesis of the photocatalysts and the mechanism of their superior CO_2 photocatalytic reduction performance are expected to inspire the design and fabrication of more advanced photocatalysts for CO_2 photocatalytic reduction.

Acknowledgements

This research is financially supported by the National Natural Science Foundation of China (No. 51578488), Zhejiang Provincial "151" Talents Program, the Program for Zhejiang Leading Team of S&T Innovation (No. 2013TD07) and Changjiang Scholar Incentive Program (Ministry of Education, China, 2009).

Electronic Supplementary Material: Supplementary material (SEM images, nitrogen adsorption–desorption curves, HRTEM images of CQDs, possible structures of oxygen doped CN, CO accumulative yields, CO_2 total conversion, CO-TPD profiles, AFM images, EIS Nyquist plots, detection of H_2O_2, H^+ production, oxygen atomic content, band gap and band-edge positions) is available in the online version of this article at https://doi.org/10.1007/s12274-019-2509-2.

References

[1] Zhou, H. L.; Qu, Y. Q.; Zeid, T.; Duan, X. F. Towards highly efficient photocatalysts using semiconductor nanoarchitectures. *Energy Environ. Sci*. **2012**, *5*, 6732–6743.

[2] Xie, S. J.; Zhang, Q. H.; Liu, G. D.; Wang, Y. Photocatalytic and photo-electrocatalytic reduction of CO_2 using heterogeneous catalysts with controlled nanostructures. *Chem. Commun*. **2016**, *52*, 35–59.

[3] Chang, X. X.; Wang, T.; Gong, J. L. CO_2 photo-reduction: Insights into CO_2 activation and reaction on surfaces of photocatalysts. *Energy Environ. Sci*. **2016**, *9*, 2177–2196.

[4] Inoue, T.; Fujishima, A.; Konishi, S.; Honda, K. Photoelectrocatalytic reduction of carbon dioxide in aqueous suspensions of semiconductor powders. *Nature* **1979**, *277*, 637–638.

[5] Habisreutinger, S. N.; Schmidt-Mende, L.; Stolarczyk, J. K. Photocatalytic reduction of CO_2 on TiO_2 and other semiconductors. *Angew. Chem., Int. Ed*. **2013**, *52*, 7372–7408.

[6] Zhou, H.; Yan, R. Y.; Zhang, D.; Fan, T. X. Challenges and perspectives in designing artificial photosynthetic systems. *Chem.—Eur. J*. **2016**, *22*, 9870–9885.

[7] Lu, L.; Wang, B.; Wang, S. M.; Shi, Z.; Yan, S. C.; Zou, Z. G. La_2O_3-modified $LaTiO_2N$ photocatalyst with spatially separated active sites achieving enhanced CO_2 reduction. *Adv. Funct. Mater*. **2017**, *27*, 1702447.

[8] White, J. L.; Baruch, M. F.; Pander III, J. E.; Hu, Y.; Fortmeyer, I. C.; Park, J. E.; Zhang, T.; Liao, K.; Gu, J.; Yan, Y. et al. Light-driven heterogeneous reduction of carbon dioxide: Photocatalysts and photoelectrodes. *Chem. Rev*. **2015**, *115*, 12888–12935.

[9] Sun, Z. X.; Wang, S. C.; Li, Q.; Lyu, M. Q.; Butburee, T.; Luo, B.; Wang, H. Q.; Fischer, J. M. T. A.; Zhang, C.; Wu, Z. B. et al. Enriching CO_2 activation sites on graphitic carbon nitride with simultaneous introduction of electron-transfer promoters for superior photocatalytic CO_2-to-fuel conversion. *Adv. Sustain. Syst*. **2017**, *1*, 1700003.

[10] Li, M. L.; Zhang, L. X.; Wu, M. Y.; Du, Y. Y.; Fan, X. Q.; Wang, M.; Zhang, L. L.; Kong, Q. L.; Shi, J. L. Mesostructured CeO_2/g-C_3N_4 nanocomposites: Remarkably enhanced photocatalytic activity for CO_2 reduction by mutual component activations. *Nano Energy* **2016**, *19*, 145–155.

[11] Low, J. X.; Yu, J. G.; Jaroniec, M.; Wageh, S.; Al-Ghamdi, A. A. Heterojunction photocatalysts. *Adv. Mater*. **2017**, *29*, 1601694.

[12] Wang, H. L.; Zhang, L. S.; Chen, Z. G.; Hu, J. Q.; Li, S. J.; Wang, Z. H.; Liu, J. S.; Wang, X. C. Semiconductor heterojunction photocatalysts: Design, construction, and photocatalytic performances. *Chem. Soc. Rev*. **2014**, *43*, 5234–5244.

[13] Dong, F.; Zhao, Z. W.; Xiong, T.; Ni, Z. L.; Zhang, W. D.; Sun, Y. J.; Ho, W. K. *In situ* construction of g-C_3N_4/g-C_3N_4 metal-free heterojunction for enhanced visible-light photocatalysis. *ACS Appl. Mater. Interfaces* **2013**, *5*, 11392–11401.

[14] Zhang, H.; Zhao, L. X.; Geng, F. L.; Guo, L. H.; Wan, B.; Yang, Y. Carbon dots decorated graphitic carbon nitride as an efficient metal-free photocatalyst for phenol degradation. *Appl. Catal. B: Environ*. **2016**, *180*, 656–662.

[15] Low, J. X.; Cheng, B.; Yu, J. G.; Jaroniec, M. Carbon-based two-dimensional layered materials for photocatalytic CO_2 reduction to solar fuels. *Energy Stor. Mater*. **2016**, *3*, 24–35.

[16] Huang, Y.; Liang, Y. L.; Rao, Y. F.; Zhu, D. D.; Cao, J. J.; Shen, Z. X.; Ho, W; Lee, S. C. Environment-friendly carbon quantum dots/$ZnFe_2O_4$ photocatalysts: Characterization, biocompatibility, and mechanisms for NO removal. *Environ. Sci. Technol*. **2017**, *51*, 2924–2933.

[17] Chen, J. W.; Shi, J. W.; Wang, X.; Cui, H. J.; Fu, M. L. Recent progress in the preparation and application of semiconductor/graphene composite photocatalysts. *Chin. J. Catal*. **2013**, *34*, 621–640.

[18] Yu, J. G.; Jin, J.; Cheng, B.; Jaroniec, M. A noble metal-free reduced graphene oxide–CdS nanorod composite for the enhanced visible-light photocatalytic reduction of CO_2 to solar fuel. *J. Mater. Chem. A* **2014**, *2*, 3407–3416.

[19] Liu, G.; Niu, P.; Sun, C. H.; Smith, S.; Chen, Z. G.; Lu, G. Q.; Cheng, H. M. Unique electronic structure induced high photoreactivity of sulfur-doped graphitic C_3N_4. *J. Am. Chem. Soc*. **2010**, *132*, 11642–11648.

[20] Zhu, Y. P.; Ren, T. Z.; Yuan, Z. Y. Mesoporous phosphorus-doped g-C_3N_4 nanostructured flowers with superior photocatalytic hydrogen evolution performance. *ACS Appl. Mater. Interfaces* **2015**, *7*, 16850–16856.

[21] Zeng, Y. X.; Liu, X.; Liu, C. B.; Wang, L. L.; Xia, Y. C.; Zhang, S. Q.; Luo, S. L.; Pei, Y. Scalable one-step production of porous oxygen-doped

g-C_3N_4 nanorods with effective electron separation for excellent visible-light photocatalytic activity. *Appl. Catal. B: Environ.* **2018**, *224*, 1–9.

[22] Fang, W. J.; Liu, J. Y.; Yu, L.; Jiang, Z.; Shangguan, W. F. Novel (Na, O) co-doped g-C_3N_4 with simultaneously enhanced absorption and narrowed bandgap for highly efficient hydrogen evolution. *Appl. Catal. B: Environ.* **2017**, *209*, 631–636.

[23] Jiang, Y. B.; Sun, Z. Z.; Tang, C.; Zhou, Y. X.; Zeng, L.; Huang, L. M. Enhancement of photocatalytic hydrogen evolution activity of porous oxygen doped g-C_3N_4 with nitrogen defects induced by changing electron transition. *Appl. Catal. B: Environ.* **2019**, *240*, 30–38.

[24] Wang, X. F.; Cheng, J. J.; Yu, H. G.; Yu, J. G. A facile hydrothermal synthesis of carbon dots modified g-C_3N_4 for enhanced photocatalytic H_2-evolution performance. *Dalton Trans.* **2017**, *46*, 6417–6424.

[25] Li, Q.; Sun, Z. X.; Wang, H. Q.; Wu, Z. B. Insight into the enhanced CO_2 photocatalytic reduction performance over hollow-structured Bi-decorated g-C_3N_4 nanohybrid under visible-light irradiation. *J. CO_2 Util.* **2018**, *28*, 126–136.

[26] Wang, H. Q.; Sun, Z. X.; Li, Q.; Tang, Q. J.; Wu, Z. B. Surprisingly advanced CO_2 photocatalytic conversion over thiourea derived g-C_3N_4 with water vapor while introducing 200–420 nm UV light. *J. CO_2 Util.* **2016**, *14*, 143–151.

[27] Thomas, A.; Fischer, A.; Goettmann, F.; Antonietti, M.; Müller, J. O.; Schlögl, R.; Carlsson, J. M. Graphitic carbon nitride materials: Variation of structure and morphology and their use as metal-free catalysts. *J. Mater. Chem.* **2008**, *18*, 4893–4908.

[28] Kang, Y. Y.; Yang, Y. Q.; Yin, L. C.; Kang, X. D.; Liu, G.; Cheng, H. M. An amorphous carbon nitride photocatalyst with greatly extended visible-light-responsive range for photocatalytic hydrogen generation. *Adv. Mater.* **2015**, *27*, 4572–4577.

[29] Fu, J. W.; Zhu, B. C.; Jiang, C. J.; Cheng, B.; You, W.; Yu, J. G. Hierarchical porous O-doped g-C_3N_4 with enhanced photocatalytic CO_2 reduction activity. *Small* **2017**, *13*, 1603938.

[30] Kang, Y. Y.; Yang, Y. Q.; Yin, L. C.; Kang, X. D.; Wang, L. Z.; Liu, G.; Cheng, H. M. Selective breaking of hydrogen bonds of layered carbon nitride for visible light photocatalysis. *Adv. Mater.* **2016**, *28*, 6471–6477.

[31] Niu, P.; Zhang, L. L.; Liu, G.; Cheng, H. M. Graphene-like carbon nitride nanosheets for improved photocatalytic activities. *Adv. Funct. Mater.* **2012**, *22*, 4763–4770.

[32] Huang, Z. F.; Song, J. J.; Pan, L.; Wang, Z. M.; Zhang, X. Q.; Zou, J. J.; Mi, W. B.; Zhang, X. W.; Wang, L. Carbon nitride with simultaneous porous network and O-doping for efficient solar-energy-driven hydrogen evolution. *Nano Energy* **2015**, *12*, 646–656.

[33] Mirtchev, P.; Henderson, E. J.; Soheilnia, N.; Yip, C. M.; Ozin, G. A. Solution phase synthesis of carbon quantum dots as sensitizers for nanocrystalline TiO_2 solar cells. *J. Mater. Chem.* **2012**, *22*, 1265–1269.

[34] Ma, T. Y.; Dai, S.; Jaroniec, M.; Qiao, S. Z. Graphitic carbon nitride nanosheet-carbon nanotube three-dimensional porous composites as high-performance oxygen evolution electrocatalysts. *Angew. Chem., Int. Ed.* **2014**, *53*, 7281–7285.

[35] Hu, Y. P.; Yang, J.; Jia, L.; Yu, J. S. Ethanol in aqueous hydrogen peroxide solution: Hydrothermal synthesis of highly photoluminescent carbon dots as multifunctional nanosensors. *Carbon* **2015**, *93*, 999–1007.

[36] Zhao, L. X.; Di, F.; Wang, D. B.; Guo, L. H.; Yang, Y.; Wan, B.; Zhang, H. Chemiluminescence of carbon dots under strong alkaline solutions: A novel insight into carbon dot optical properties. *Nanoscale* **2013**, *5*, 2655–2658.

[37] Hu, S. L.; Tian, R. X.; Wu, L. L.; Zhao, Q.; Yang, J. L.; Liu, J.; Cao, S. R. Chemical regulation of carbon quantum dots from synthesis to photocatalytic activity. *Chem.—Asian J.* **2013**, *8*, 1035–1041.

[38] Li, J. H.; Shen, B.; Hong, Z. H.; Lin, B. Z.; Gao, B. F.; Chen, Y. L. A facile approach to synthesize novel oxygen-doped g-C_3N_4 with superior visible-light photoreactivity. *Chem. Commun.* **2012**, *48*, 12017–12019.

[39] She, X. J.; Liu, L.; Ji, H. Y.; Mo, Z.; Li, Y. P.; Huang, L. Y.; Du, D. L.; Xu, H.; Li, H. M. Template-free synthesis of 2D porous ultrathin nonmetal-doped g-C_3N_4 nanosheets with highly efficient photocatalytic H_2 evolution from water under visible light. *Appl. Catal. B: Environ.* **2016**, *187*, 144–153.

[40] Liu, J. H.; Zhang, T. K.; Wang, Z. C.; Dawson, G.; Chen, W. Simple pyrolysis of urea into graphitic carbon nitride with recyclable adsorption and photocatalytic activity. *J. Mater. Chem.* **2011**, *21*, 14398–14401.

[41] Qiu, P. X.; Xu, C. M.; Chen, H.; Jiang, F.; Wang, X.; Lu, R. F.; Zhang, X. R. One step synthesis of oxygen doped porous graphitic carbon nitride with remarkable improvement of photo-oxidation activity: Role of oxygen on visible light photocatalytic activity. *Appl. Catal. B: Environ.* **2017**, *206*, 319–327.

[42] Bu, Y. Y.; Chen, Z. Y. Effect of oxygen-doped C_3N_4 on the separation capability of the photoinduced electron-hole pairs generated by O-C_3N_4@TiO_2 with quasi-shell-core nanostructure. *Electrochim. Acta* **2014**, *144*, 42–49.

[43] Li, H. J.; Sun, B. W.; Sui, L.; Qian, D. J.; Chen, M. Preparation of water-dispersible porous g-C_3N_4 with improved photocatalytic activity by chemical oxidation. *Phys. Chem. Chem. Phys.* **2015**, *17*, 3309–3315.

[44] Yang, D. X.; Velamakanni, A.; Bozoklu, G.; Park, S; Stoller, M.; Piner, R. D.; Stankovich, S.; Jung, I.; Field, D. A.; Ventrice Jr, C. A. et al. Chemical analysis of graphene oxide films after heat and chemical treatments by X-ray photoelectron and micro-Raman spectroscopy. *Carbon* **2009**, *47*, 145–152.

[45] Wang, X. P.; Chen, Y. X.; Fu, M.; Chen, Z. H.; Huang, Q. L. Effect of high-voltage discharge non-thermal plasma on g-C_3N_4 in a plasma-photocatalyst system. *Chin. J. Catal.* **2018**, *39*, 1672–1682.

[46] Li, H. T.; He, X. D.; Kang, Z. H.; Huang, H.; Liu, Y.; Liu, J. L.; Lian, S. Y.; Tsang, C. H. A.; Yang, X. B.; Lee, S. T. Water-soluble fluorescent carbon quantum dots and photocatalyst design. *Angew. Chem., Int. Ed.* **2010**, *49*, 4430–4434.

[47] Fusco, C.; Casiello, M.; Catucci, L.; Comparelli, R.; Cotugno, P.; Falcicchio, A.; Fracassi, F.; Margiotta, V.; Moliterni, A.; Petronella, F. et al. TiO_2@PEI-grafted-MWCNTs hybrids nanocomposites catalysts for CO_2 photoreduction. *Materials* **2018**, *11*, 307.

[48] Ou, H. H.; Yang, P. J.; Lin, L. H.; Anpo, M.; Wang, X. C. Carbon nitride aerogels for the photoredox conversion of water. *Angew. Chem., Int. Ed.* **2017**, *56*, 10905–10910.

[49] Szanyi, J.; Kwak, J. H. Dissecting the steps of CO_2 reduction: 1. The interaction of CO and CO_2 with γ-Al_2O_3: An *in situ* FTIR study. *Phys. Chem. Chem. Phys.* **2014**, *16*, 15117–15125.

[50] Zhang, B.; Zhao, T. J.; Feng, W. J.; Liu, Y. X.; Wang, H. H.; Su, H.; Lv, L. B.; Li, X. B.; Chen, J. S. Polarized few-layer g-C_3N_4 as metal-free electrocatalyst for highly efficient reduction of CO_2. *Nano Res.* **2018**, *11*, 2450–2459.

[51] Li, X. C.; Wu, M.; Lai, Z. H.; He, F. Studies on nickel-based catalysts for carbon dioxide reforming of methane. *Appl. Catal. A: Gen.* **2005**, *290*, 81–86.

[52] Ong, W. J.; Tan, L. L.; Chai, S. P.; Yong, S. T.; Mohamed, A. R. Surface charge modification via protonation of graphitic carbon nitride (g-C_3N_4) for electrostatic self-assembly construction of 2D/2D reduced graphene oxide (rGO)/g-C_3N_4 nanostructures toward enhanced photocatalytic reduction of carbon dioxide to methane. *Nano Energy* **2015**, *13*, 757–770.

[53] Zhao, Y. L.; Wei, Y. C.; Wu, X. X.; Zheng, H. L.; Zhao, Z.; Liu, J.; Li, J. M. Graphene-wrapped Pt/TiO_2 photocatalysts with enhanced photogenerated charges separation and reactant adsorption for high selective photoreduction of CO_2 to CH_4. *Appl. Catal. B: Environ.* **2018**, *226*, 360–372.

[54] Tang, Q. J.; Sun, Z. X.; Wang, P. L.; Li, Q.; Wang, H. Q.; Wu, Z. B. Enhanced CO_2 photocatalytic reduction performance on alkali and alkaline earth metal ion-exchanged hydrogen titanate nanotubes. *Appl. Surf. Sci.* **2019**, *463*, 456–462.

[55] Peng, Y. H.; Wang, L. B.; Luo, Q. Q.; Cao, Y.; Dai, Y. Z.; Li, Z. L.; Li, H. L.; Zheng, X. S.; Yan, W. S.; Yang, J. L. et al. Molecular-level insight into how hydroxyl groups boost catalytic activity in CO_2 hydrogenation into methanol. *Chem* **2018**, *4*, 613–625.

[56] Li, Y. F.; Jin, R. X.; Xing, Y.; Li, J. Q.; Song, S. Y.; Liu, X. C.; Li, M.; Jin, R. C. Macroscopic foam-like holey ultrathin g-C_3N_4 nanosheets for drastic improvement of visible-light photocatalytic activity. *Adv. Energy Mater.* **2016**, *6*, 1601273.

[57] Fang, S.; Xia, Y.; Lv, K. L.; Li, Q.; Sun, J.; Li, M. Effect of carbon-dots modification on the structure and photocatalytic activity of g-C_3N_4. *Appl. Catal. B: Environ.* **2016**, *185*, 225–232.

[58] Delgado, E. R.; Alves, L. A.; Verly, R. M.; De Lemos, L. R.; De Mesquita, J. P. Purification, selection, and partition coefficient of highly oxidized carbon dots in aqueous two-phase systems based on polymer-salt pairs. *Langmuir* **2017**, *33*, 12235–12243.

[59] Hong, Y. Z.; Shi, J. Y.; Shi, W. D.; Fang, Z. Y.; Chen, R. J.; Huang, Y. Y. A facile and scalable route for synthesizing ultrathin carbon nitride nanosheets with efficient solar hydrogen evolution. *Carbon* **2018**, *136*, 160–167.

[60] Wu, P.; Wang, J. R.; Zhao, J.; Guo, L. J.; Osterloh, F. E. Structure defects in g-C_3N_4 limit visible light driven hydrogen evolution and photovoltage. *J. Mater. Chem. A* **2014**, *2*, 20338–20344.

[61] Dong, G. H.; Jacobs, D. L.; Zang, L.; Wang, C. Y. Carbon vacancy

regulated photoreduction of NO to N_2 over ultrathin g-C_3N_4 nanosheets. *Appl*. *Catal*. *B*: *Environ*. **2017**, *218*, 515–524.

[62] Li, Q.; Gao, S.; Hu, J.; Wang, H. Q.; Wu, Z. B. Superior NO_x photocatalytic removal over hybrid hierarchical Bi/BiOI with high non-NO_2 selectivity: Synergistic effect of oxygen vacancies and bismuth nanoparticles. *Catal*. *Sci*. *Technol*. **2018**, *8*, 5270–5279.

[63] Zhao, H. X.; Chen, X. Y.; Li, X. T.; Shen, C.; Qu, B. C.; Gao, J. S.; Chen, J. W.; Quan, X. Photoinduced formation of reactive oxygen species and electrons from metal oxide-silica nanocomposite: An EPR spin-trapping study. *Appl*. *Surf*. *Sci*. **2017**, *416*, 281–287.

[64] Yin, W. J.; Bai, L. J.; Zhu, Y. Z.; Zhong, S. X.; Zhao, L. H.; Li, Z. Q.; Bai, S. Embedding metal in the interface of a p-n heterojunction with a stack design for superior Z-scheme photocatalytic hydrogen evolution. *ACS Appl*. *Mater*. *Interfaces* **2016**, *8*, 23133–23142.

[65] Putri, L. K.; Ng, B. J.; Ong, W. J.; Lee, H. W.; Chang, W. S.; Chai, S. P. Engineering nanoscale p–n junction via the synergetic dual-doping of p-type boron-doped graphene hybridized with n-type oxygen-doped carbon nitride for enhanced photocatalytic hydrogen evolution. *J*. *Mater*. *Chem*. *A* **2018**, *6*, 3181–3194.

[66] Wu, J. C. S. Photocatalytic reduction of greenhouse gas CO_2 to fuel. *Catal*. *Surv*. *Asia* **2009**, *13*, 30–40.

[67] Xie, T. P.; Liu, Y.; Wang, H. Q.; Wu, Z. B. Layered $MoSe_2/Bi_2WO_6$ composite with P-N heterojunctions as a promising visible-light induced photocatalyst. *Appl*. *Surf*. *Sci*. **2018**, *444*, 320–329.

[68] Dimitrijevic, N. M.; Vijayan, B. K.; Poluektov, O. G.; Rajh, T.; Gray, K. A.; He, H. Y.; Zapol, P. Role of water and carbonates in photocatalytic transformation of CO_2 to CH_4 on titania. *J*. *Am*. *Chem*. *Soc*. **2011**, *133*, 3964–3971.

[69] Rajalakshmi, K.; Jeyalakshmi, V.; Krishnamurthy, K. R.; Viswanathan, B. Photocatalytic reduction of carbon dioxide by water on titania: Role of photophysical and structural properties. *Indian J*. *Chem*. **2012**, *51A*, 411–419.